Analysis of X-ray Tensor Tomography: A Phantom Study

Master Project in Advanced Optical Technologies

submitted
by

Florian Schiffers

born 21.03.1992 in Würzburg

Written at

Lehrstuhl für Mustererkennung (Informatik 5)
Department Informatik
Friedrich-Alexander-Universität Erlangen-Nürnberg.

Advisor: Prof. Dr.-Ing. habil. Andreas Maier, Dr.-Ing. Christian Riess, M. Sc. Shiyang Hu

Started: 01.02.2016

Finished: 01.05.2016

Ich versichere, dass ich die Arbeit ohne fremde Hilfe und ohne Benutzung anderer als der angegebenen Quellen angefertigt habe und dass die Arbeit in gleicher oder ähnlicher Form noch keiner anderen Prüfungsbehörde vorgelegen hat und von dieser als Teil einer Prüfungsleistung angenommen wurde. Alle Ausführungen, die wörtlich oder sinngemäß übernommen wurden, sind als solche gekennzeichnet.

Die Richtlinien des Lehrstuhls für Studien- und Diplomarbeiten habe ich gelesen und anerkannt, insbesondere die Regelung des Nutzungsrechts.

Erlangen, den 01.Mai.2016

Abstract

In recent years tomographic reconstruction methods for interferometric X-ray imaging have drawn attention to the X-ray imaging community. An unresolved task remains in reconstruction of the anisotropic part of X-ray dark-field signals. Many attempts have been made to tackle this issue [1–4]. Among them X-ray Tensor Tomography (XTT) [3] recovers tensorial information by fully sampling the 3-D imaging space.

In this work, we investigate the behavior of XTT. In particular, we examine the influence of number of chosen scatter directions with respect to accuracy and convergence. Additionally, we analyze the algorithm's capability to reconstruct complex fiber structures with only two tomographic trajectories. The experiments are performed on numerical phantom data.

Contents

1 Introduction **3**

2 Previous Work **5**

3 Implemented Method **7**

3.1 Gradient Descent 8

3.2 Gradient Descent with Zero-Constraint 10

3.3 Extraction of Tensorial Information 10

4 Methods **11**

4.1 Number and Definition of Scatter Directions 11

4.2 Parallel Beam Geometry 12

4.3 Tensor Tomography with two Trajectories 13

4.4 Visualization of Data 13

4.5 Phantom Data 13

4.6 Creation of Dark-Field Images 15

5 Results **19**

5.1 Reconstruction Results 19

5.2 Gradient Descent Analysis 21

5.3 Influence of Scatter Directions 22

6 Discussion and Outlook **25**

6.1 Discussion 25

6.2 Outlook 25

List of Figures **27**

Bibliography **28**

Chapter 1

Introduction

X-ray attenuation imaging has been one of the most important imaging techniques to observe contrast images between highly and lowly absorbing structures. However, from a physical point of view, the electro-magnetic wave character of X-rays is hereby not fully exploited. By using new measurement approaches, in means of interferometric techniques known from the fields of optics [5], more information can be gained.

Even though extensive research has been carried out on imaging the phase-shift experienced by an X-ray when passing through a specimen [6–10], these techniques were limited to physic laboratories due to the requirement of coherent X-ray illumination. A breakthrough was made when Pfeiffer et al. [11] demonstrated a novel setup for X-ray grating interferometry [12, 13] comprising an ordinary X-ray tube combined with special gratings.

With this interferometric setup three signal components are extracted, namely the already known absorption and additionally the phase-contrast and the dark-field component. Examples of each modality are given in figure 1.1.

Recently, efforts were made to find reasonable methods for a volumetric reconstruction of the dark-field signal. A straight-forward approach to recover three-dimensional scalar data, comparable to attenuation CT [14], is limited to isotropic scattering, since only a scalar value related to a scattering strength is recovered [15]. Despite this drawback, it has shown to give beneficial results for applications where the other two signals, attenuation and phase-contrast fail to provide high contrast signals [15]. Thus one has powerful arguments to believe that tomographic reconstruction of the anisotropic scattering components is able to provide additional insights, helpful in medical diagnostics or material sciences [16].

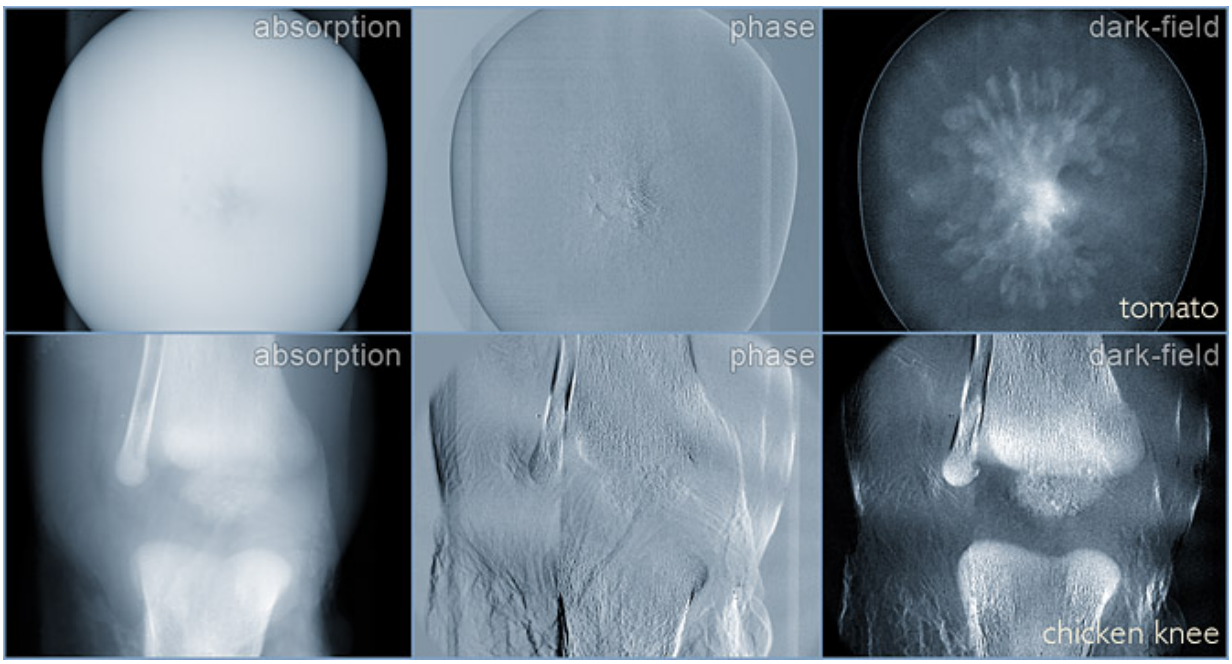

Figure 1.1: A tomato and a knee sample from (a) absorption image, (b) phase-contrast image, (c) dark-field image. Image taken from `http://bruker-microct.com/company/research.htm` (date: 04/15/2016)

Chapter 2

Previous Work

X-ray absorption tomography has been one of the most important diagnostic modalities over the last decades. A lot of research has been conducted on optimizing and analyzing reconstruction algorithms. The most popular method among them is the Filtered Back Projection (FBP) [14].

With the final breakthrough of interferometric X-ray imaging in 2006 it was not long until the X-ray reconstruction community started to apply methods related to FBP for phase-contrast tomography with remarkable results [17, 18]. Their basic idea is to build a physical model for the differential phase-contrast signal inspired by the Beer-Lambert Law [19]. Under this premise FBP can be applied almost directly to the phase-contrast images.

The first approaches applying computed tomography on the dark-field signal have been published by Bech et al. [15]. Assuming the visibility signal to decay comparable to the Beer-Lambert law, they introduce the material-dependent Linear Diffusion Coefficient (LDC). In a straight-forward thinking they performed FBP-like reconstruction, which is naturally constrained to isotropic dark-field scattering due to scalar representation of its signal.

Around the same time Jensen et al. [16] and later Revol et al. [20] demonstrated the directional dependence of the X-ray dark-field signal. First efforts to consider this particular property of the dark-field signal were made by Malecki et al. [3] and Bayer et al. [2].

Malecki was able to reconstruct three dimensional structural information out of a wooden block sample with images coming from a full tomographic dataset. In earlier work he introduced a physical model inspired by the well-known Beer-Lambert Law for X-ray attention imaging comprising artificial scattering directions [21]. His work was carried on and led to a very recent publication by Vogel et al. [4]. By constraining the reconstructed parameters they receive very promising results on real objects like tree branches and teeth.

Whereas Malecki's method does not differentiate between isotropic and anisotropic contri-

butions, Bayer et al. [2] successfully reconstructed both, scalar and vectorial components using data from only one tomographic scan. Since the proposed method reconstructs only the projected angle from 3D local orientation onto the plane defined by the sensor's trajectory, the vectorial component remains in a 2D plane. This drawback was overcome by Hu et al. [1] using a second tomographic scan perpendicular to the first.

The latter method has shown that the specimen's micro orientation can principally be reconstructed by just two tomographic scans. This gives rise to the question if the method proposed by Malecki is able to achieve similar results under equal conditions. This issue will be dealt with among others in the following.

Chapter 3

Implemented Method

In preceding work [20, 22], a physical model of directional dark-field imaging was developed. Similar to their predecessors, the model shows resemblance with the Beer-Lambert Law, yet restricted to a two-dimensional reconstruction.

Malecki generalizes this idea by introducing a finite set of artificial scattering directions in his model:

$$D(x,y) = \exp\left[-\int \sum_i \left\langle \widetilde{\boldsymbol{\epsilon}}_i\left(\boldsymbol{s},x,y,z\right),\boldsymbol{t}\right\rangle^2 dz\right]. \tag{3.1}$$

Here, x, y and z are given by the specimen's coordinate system. D stands for the measured dark-field signal, $\langle\cdot,\cdot\rangle$ is the inner product, $\boldsymbol{s} \in \mathbb{R}^3$ is the incoming beam and $\boldsymbol{t} \in \mathbb{R}^3$ is the interferometer's sensitivity vector. The dependence of the dark-field signal on the direction of the incoming beam, is hereby modeled by the notional scatter directions $\widetilde{\boldsymbol{\epsilon}}_i$, which contributions are subject to reconstruction.

Their absolute value describes the effective scattering strength of a voxel for each defined scatter direction. One remarkable point is that the choice of number and orientation of the scatter directions has been rather arbitrary and no research has been conducted on this question until now. Furthermore, he proposed ellipsoid fitting onto reconstruction data providing tensorial information on the local scattering.

In subsequent work followed by Vogel [4] a more elegant fitting algorithm based on Principal Component Analysis (PCA) was introduced. Additionally, they presented a more generic algorithm for reconstruction comprising two approaches to constrain the obtained scatter strengths by enforcing them to form ellipsoidal shapes.

3.1 Gradient Descent

Based on [3] Vogel et al. [4] reformulated a forward-projection model for the dark-field:

$$d_j = \exp\left[- \int_{L_j} \sum_k \left\langle \left| \hat{\boldsymbol{I}}_j \times \hat{\boldsymbol{\epsilon}}_k \right| \zeta_k(\boldsymbol{x}) \hat{\boldsymbol{\epsilon}}_k, \hat{\boldsymbol{t}}_j \right\rangle^2 dx \right]. \tag{3.2}$$

Where d_j denotes the j-th dark-field signal measured by the ray L_j and its normalized direction $\hat{\boldsymbol{I}}_j$. Note that one specific pixel of the detector image of one specific pose is represented by the independent measurement j. Thus the index $j = 1, .., J$ has the length of $J = M \cdot N \cdot P$, where M and N are the detector's resolution and P is the number of acquired projections. $\hat{\boldsymbol{t}}_j$ denotes the normalized sensitivity direction, defined to be orthogonal to the grating lines and parallel to the grating's surface.

By reformulating this equation one can separate this model into the unknown part, the squared scattering coefficients $\eta_k(x) := \zeta_k(x)^2$, and a constant weight factor, which is only dependent on the setup's geometry:

$$v_{kj} = \left(\left| \hat{\boldsymbol{I}}_j \times \hat{\boldsymbol{\epsilon}}_k \right| \left\langle \hat{\boldsymbol{\epsilon}}_k, \hat{\boldsymbol{t}}_j \right\rangle \right)^2 \tag{3.3}$$

Inserting and taking the logarithm leads to the following measurement:

$$m_j := -\ln d_j = \int_{L_j} \sum_k v_{kj} \cdot \eta_k(x) dx = \sum_k v_{kj} \int_{L_j} \eta_k(x) dx \tag{3.4}$$

In a discretized manner the line-integrals are rewritten by a scalar product

$$m_j = \sum_k v_{kj} \langle \boldsymbol{a}_j, \boldsymbol{\eta}_k \rangle = \sum_k v_{kj} \boldsymbol{a}_j^T \boldsymbol{\eta}_k. \tag{3.5}$$

$\boldsymbol{\eta}_k \in \mathbb{R}^I$ is a vector containing the squared coefficients for the k-th scatter direction for each voxel element (I is the number of voxel elements) and $\boldsymbol{a}_j \in \mathbb{R}^I$ is the j-th row of the measurement matrix $\boldsymbol{A}$ which is defined in the same manner as in attenuation reconstruction [14]. Introducing the dark-field measurement vector $\boldsymbol{m} = (m_j)_{j=1,...,J}$ and a diagonal scaling matrix $\boldsymbol{D_k} = diag(v_{k1}, v_{k2}, ...)$, one defines a huge linear equation system $\boldsymbol{H}$ (see also [4]):

$$\boldsymbol{m} = (\boldsymbol{D_1 A}, \boldsymbol{D_2 A}, ..., \boldsymbol{D_k A}) \begin{pmatrix} \boldsymbol{\eta}_1 \\ \boldsymbol{\eta}_2 \\ \vdots \\ \boldsymbol{\eta}_k \end{pmatrix} \tag{3.6}$$

Redefining $\boldsymbol{H} := (\boldsymbol{D_1 A}, \boldsymbol{D_2 A}, ..., \boldsymbol{D_k A})$ and $\boldsymbol{s}^T := (\boldsymbol{\eta}_1, \boldsymbol{\eta}_1, ..., \boldsymbol{\eta}_k)$ leads finally to the following clear and compact representation of the latter system:

$$\boldsymbol{m} = \boldsymbol{H s} \tag{3.7}$$

Linear equation systems are often solved by computing an approximate solution of the least squares minimization problem. Let us recall that solving the prior derived equation is equal to minimizing the following functional.

$$f(\boldsymbol{s}) = \|\boldsymbol{H s} - \boldsymbol{m}\|_2^2 = (\boldsymbol{H s} - \boldsymbol{m})^T \cdot (\boldsymbol{H s} - \boldsymbol{m}) \tag{3.8}$$

A common and easy-to-implement algorithm is the gradient descent, which is an iterative method, gradually approximation the solution. Starting with an initial solution, one calculates the next iteration by following update rule:

$$\boldsymbol{s}^{k+1} = \boldsymbol{s}^k - t^k \nabla f(\boldsymbol{s}^k), \tag{3.9}$$

where t^k denotes the step length for each step and ∇f the gradient, which is calculated as follows:

$$\nabla f(\boldsymbol{s}) = 2 \cdot \boldsymbol{H}^T(\boldsymbol{H s - m}) \tag{3.10}$$

In order to further analyze the meaning of the gradient step, let us recall that H is the huge XTT system matrix which was formed by multiplication of the weighting factors of each scatter direction with the attenuation system Matrix $\boldsymbol{A}$. Subsequently, by looking at the multiplication of one submatrix $\boldsymbol{D_j A}$ in $\boldsymbol{H}$ with its corresponding scatter coefficient vector $s_j = \eta_j$, we find that this is nothing more than a weighted forward projection. Forward projection of all scatter directions is then equal to calculating the dark-field signals of the current reconstruction result. In the same manner the transpose $\boldsymbol{H}^T$ describes a back projection into the volume spanned by the particular scatter direction.

The algorithm can be rephrased into simpler words: Iteratively calculate the difference between the measured dark-field and the forward-projected reconstruction result and project this difference back into the 3D tensor space.

3.2 Gradient Descent with Zero-Constraint

Since the optimal step length of the gradient descent cannot be calculated or approximated properly without high computational effort, this algorithm would require handcrafted adaption of parameters and additionally might run into local minima. In order to circumvent these numerical instabilities we make use of the concept of the zero-constrained gradient descent which was already introduced by Bayer et al. [2]. This approach finds its justification in the fact that one can assume that scattering is only observed in real objects and is zero in the air phase.

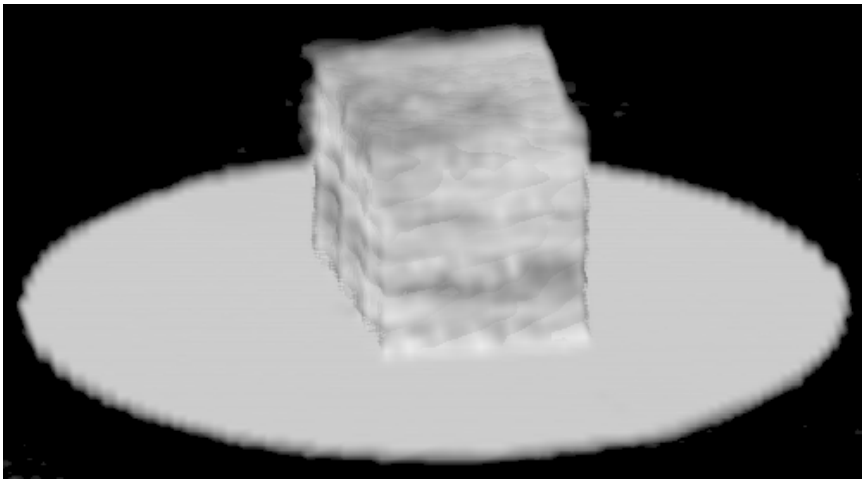

Figure 3.1: Reconstructed absorption image of the wooden block example used for zero constraint.

For real data the zero constrain can be obtained by reconstruction of the already available attenuation signals acquired during the phase-stepping procedure in Talbot-Lau interferometry [11]. An example is given in figure 3.1. In the case of phantom data the zero constrain is already known due to its modeling process.

3.3 Extraction of Tensorial Information

For each voxel the scattering coefficients η_k for the sampled scatter directions $\widetilde{\epsilon_i}$ are reconstructed by XTT. Different approaches have been proposed to extract the tensorial information by fitting an ellipsoid onto the latter [3, 4]. Following the argument of Vogel we use the PCA to extract the ellipsoid's parameters for reasonable computation time [23]. Hereby a set of 2K points in 3D space is generated by scaling the scatter directions $\widetilde{\epsilon_i}$ with the reconstructed coefficients. With addition of the same points, just scaled with -1, one ensures that the point set forms an actual point set comprising ellipsoidal shape. More detailed information can be found in [4].

Chapter 4

Methods

In the following, methods implemented in our realization of XTT are presented. We first introduce a novel method to calculate the scatter directions, followed by depiction of the experimental setup in simulation. We further explain how data are visualized and conclude this chapter with definition and generation of numeric phantom data.

4.1 Number and Definition of Scatter Directions

Malecki introduces the scattering directions as abstract entities without any further physical justification. Moreover, Vogel notes that the exact orientation of the sampling direction is rather arbitrary [4] and no prior knowledge is required to define those directions. Additionally, as scattering is assumed to be a symmetric property, only one hemisphere is sampled.

In the evaluation of Malecki's wooden block sample only 7 directions are chosen, the cube's edges and diagonals, but he states that for unknown objects a larger number is required. Since an increasing number directly correlates to longer processing time, which becomes an important factor for large data sizes, we are particularly interested how this number effects the quality of reconstruction. Additionally, the scatter directions should sample the angular range as equidistantly as possible. A manual choice of those, especially for an arbitrary number of scattering directions, is cumbersome. Thus we make use of the method proposed by Saff [24] to generate N points on a hemisphere, which will serve as the scatter directions. An example for a different numbers of sampled points is given in figure 4.1.

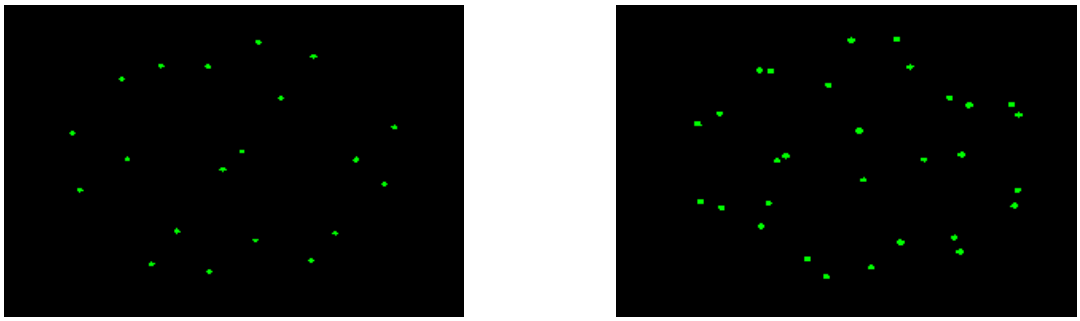

(a) N=10 (b) N=15

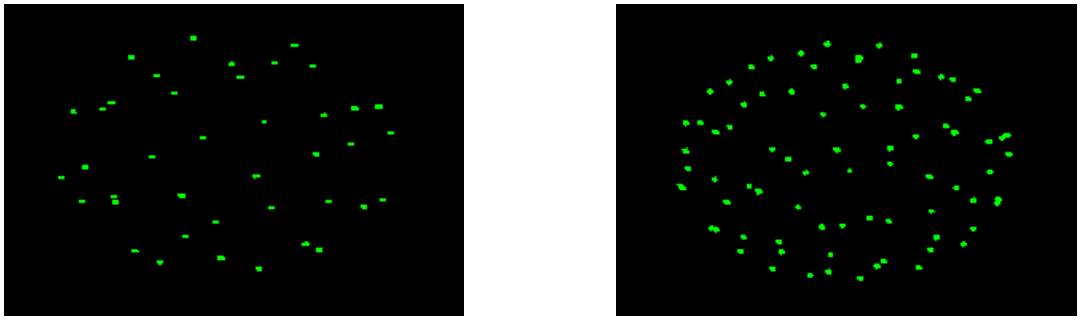

(c) N=20 (d) N=40

Figure 4.1: Points are randomly sampled on the hemisphere with the method proposed by Saff [24]. While fitting the ellipsoid in a later processing step, every point of the hemisphere is mirrored. For this reason we display here the whole sampled sphere, and not only the hemisphere.

4.2 Parallel Beam Geometry

To perform our numeric experiments we have implemented XTT in parallel beam geometry [14]. A parallel beam geometry is usually valid, if the geometric magnification M, defined by the ratio of the source-object distance and source-detector distance, approaches unity [25]. The experiments performed by ECAP provide a value of roughly unity with $M = 180/160 = 1.125$, thus using parallel beam geometry is proper.

The projector and back-projector algorithms have been implemented according to the models introduced in section 3.1. Both ray-driven and voxel-driven algorithms have been implemented for computation on the CPU, where the voxel-driven has shown to give tremendous time advantages [26]. We want to remark that GPU based methods are beneficial since the projector operators are highly parallelizable.

4.3 Tensor Tomography with two Trajectories

Malecki et al. [3] and Vogel et al. [4] sample the whole angular spectrum of the tomographic sphere by using an eulerian cradle. For many applications a full tomographic scan is not feasible due to mechanical restrictions or instabilities. However, projections from only two different tomographic scans are easily obtained with state-of-the-art CT systems. For this reason we investigate the behavior of XTT for two trajectories.

4.4 Visualization of Data

Since every sample position contains tensorial data, which cannot be visualized by traditional 3D images or even vector fields, visualization of the reconstructed data is challenging. Malecki proposes two ways of data visualization: On the one side, he extracts the fiber directions, defined as the ellipsoid's shortest half-axis, and plots them as a vector field. On the other side, he encodes the fiber direction by color. A drawback lies in the loss of information: It is not possible to convey the tensorial character in this representation. Vogel takes up on this point and plots a color encoded ellipsoid at every sample position. While the tensorial character is hereby maintained, it becomes confusing when high resolution data are displayed, since no meaningful information is conveyed to the user. Eventually he proposes a streamline visualization [4] due to their interest in fibrous objects. We will restrict ourselves to plot the fiber directions, since they convey the most meaningful message, at least regarding the type of objects we were considering.

4.5 Phantom Data

We design our phantom to hold an anisotropic scatter distribution, in other words: At every point of the object, scattering is dominant in a particular direction. In order to create an analytical phantom containing anisotropic scatter information a tensor field needs to be defined: At every spatial position, a specific ellipsoid is defined by its three half-axes and their magnitudes. To create this ellipsoid out of a set of given fiber directions, we define a ratio between the magnitude of the smallest half-axis, defining the dominant fiber directions, and the remaining two. The ellipsoid is assumed to be symmetric, which leads to equal eigenvalues for the second and third half-axes. Since no real reconstruction data are publicly available, we estimate this ratio out of the images provided in Vogel [4].

We evaluated our experiments on two well-defined phantoms. First, we rebuilt the wooden-

block sample, see figure 4.2, which was used for the first dark-field orientation experiments [2, 3]. Due to its simplicity - the used wooden-block contains only two different layers of well-defined orientations and homogeneous material - the phantom is not representative to show that two trajectories suffice for XTT.

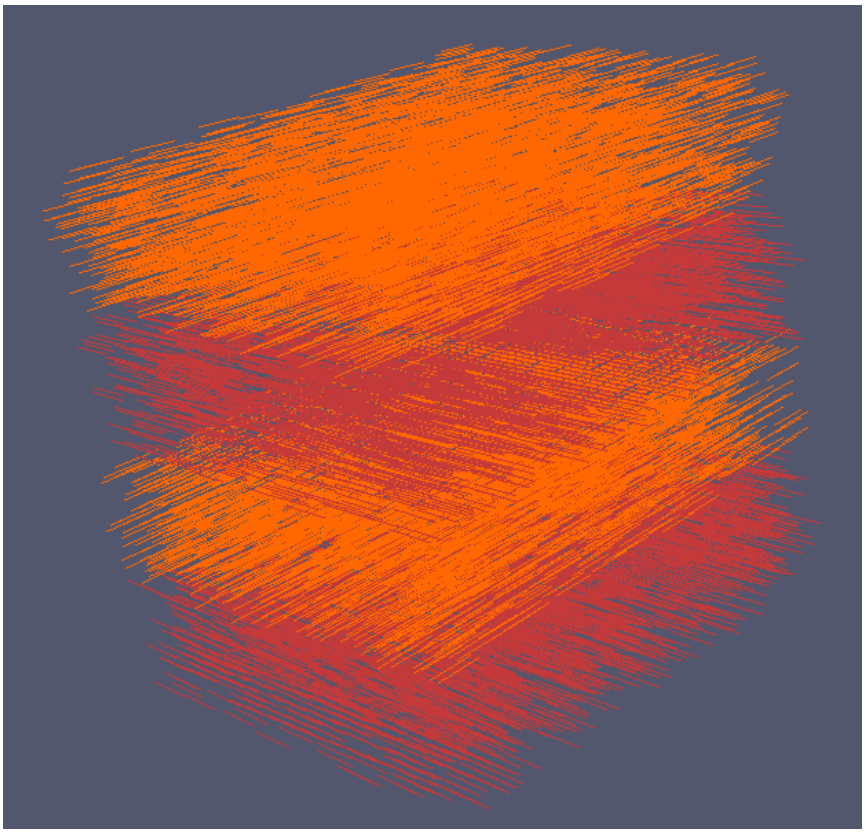

Figure 4.2: Visualization of the wooden-block sample. The phantom consists of four layers with two distinct directions. The first and the third layer have the same direction, while the second and the fourth are perpendicular. The directions are defined by the ellipsoid's smallest half-axis.

With the second phantom, we modeled two ropes, fabricated from densely packed fibers, which are piled together to form an intertwined helical structure. The fiber directions are then defined tangential to the phantom's skeleton in the lateral plane. To model a non-homogeneous scattering strength, we increase its z-component linearly with the current rope's height starting at 0. The centerline and fiber directions of the rope are defined by following equations, while the second rope is generated by adding an 180 degree shift in the lateral plane:

$$x = R \cdot \cos \alpha_{max} \cdot t$$

$$y = R \cdot \sin \alpha_{max} \cdot t$$

$$z = z_0 + L \cdot t^2$$

$$d_x = s \cdot sin\alpha_{max} \cdot t$$

$$d_y = -s \cdot \cos\alpha_{max} \cdot t$$

$$d_z = s \cdot t$$

$$t \in [0, 1], \tag{4.1}$$

where x,y and z denote the spatial coordinates and $\mathbf{d} = (d_x, d_y, d_z)^T$ is the corresponding fiber direction.

Finally, after a proper definition of the tensor field, one needs to calculate the scatter weights to form the actual phantom. By definition, these are the projections onto the ellipsoid's surface and are extracted by applying the hard ellipsoid constraint proposed in Vogel [4].

4.6 Creation of Dark-Field Images

By creation of a pure phantom volume containing just its scatter weights, no dark-field images are generated yet. By applying the physical model proposed by Malecki [3] one is able to define a proper forward propagation model to create the dark-field projection images. We want to stress that this method can only prove self-consistency of the proposed algorithm. A more physical justification of XTT is possible by applying a wave-simulation propagation algorithm, as proposed by Malecki [27] or Ritter [28]. As none of the simulation software have been available to us, we restrict ourselves to prove the latter mentioned self-consistency.

In order to create the most reliable projections images the angular spectrum spanned by the arbitrarily chosen scatter directions has to be sampled as best as possible. We chose a significantly higher number of scatter directions for creation of the dark-field projections images to avoid possible sampling errors.

The dark-field images of the wooden-block and the rope phantom are displayed in sinogram representation in the figures 4.3, 4.4 and 4.5. Two major differences of the dark-field signal in comparison to traditional absorption imaging are observed. First, since absorption imaging cannot differentiate between the orientation of a specimen, one would observe the same transmission images for layer 1 and layer 2 in the wooden-block sample. Thus computed tomography would reconstruct a homogeneous object and directional information is lost. Secondly, the dark-field's dependency on the direction of the incoming beam can be observed in the sinogram images. At layer 1's highest dark-field contrast, layer 2 shows the lowest contrast. The inverted behavior is

observed at an $\pi/2$ rotated detector position, see figure 4.3. Similar behavior is observed for the more complex sinograms of the rope phantom. Directions with a maximum dark-field signal and the $\pi/2$ rotated complementary with almost no signal strength are again observed.

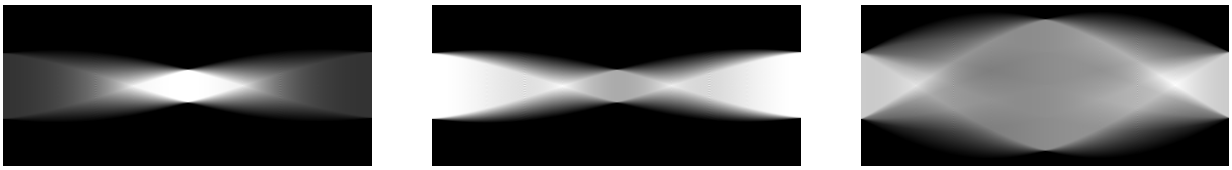

(a) Layer 1, Trajectory 1. (b) Layer 2, Trajectory 1. (c) Trajectory 2.

Figure 4.3: Sinogram of the wooden-block phantom for two trajectories. The second is perpendicular to the first. For the first trajectory, the sinograms of the two layers are different, because their internal scattering structure is different. For the second trajectory, the wooden-block sample creates the same signal for every possible ray due to its homogeneity: One observes the same sinogram for every z-slice.

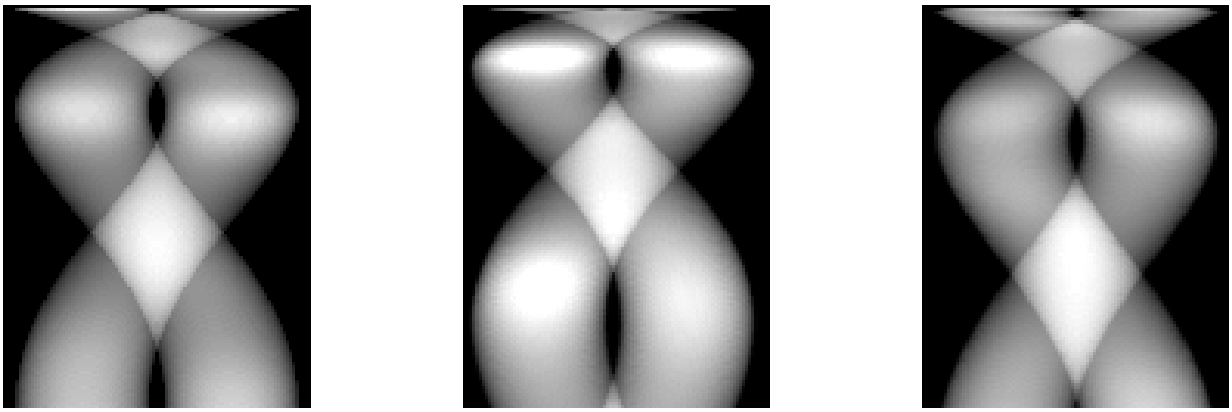

(a) View 1 (b) View 2 (c) View 3

Figure 4.4: dark-field images of the rope phantom for trajectory 1.

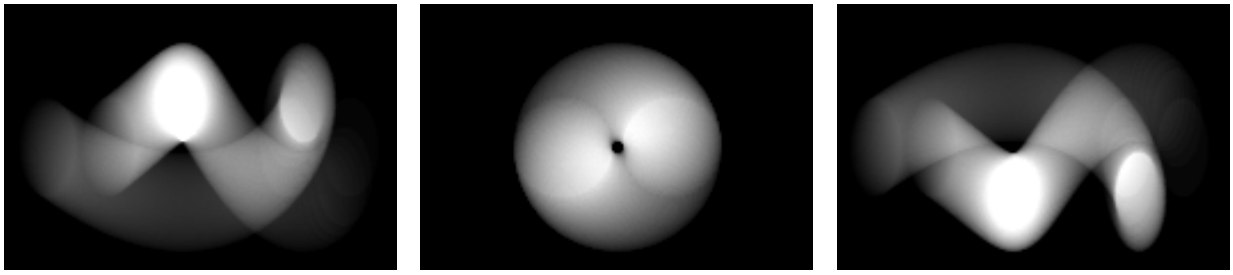

(a) View 1 (b) View 2 (c) View 3

Figure 4.5: dark-field images of the rope phantom for trajectory 2.

Chapter 5

Results

In the following results are presented. We show XTT reconstruction of phantom data (see section 4.5) with only two trajectories. Then, we demonstrate the influence of choice of scatter directions on reconstruction results.

5.1 Reconstruction Results

Since XTT was introduced on experiments conducted with an eulerian cradle enabling a full tomographic scan [3] no evaluation with only two mutually perpendicular trajectories is known to us. We performed XTT on the wooden-block phantom (Figure 5.1) and the rope phantom (Figure 5.2), where the underlying dark-field images were generated by forward-projection of the phantoms on the latter two traditional trajectories. For each trajectory a 180 degree scan with an angular step of one degree was performed. In total, 360 projection images (180 per trajectory) were obtained and used for reconstruction.

For the wooden-block phantom the fiber directions were reconstructed correctly in the most parts. At the boundaries the fiber directions are bent, which is probably due to a non-steady transition in the zero-constraint. The reconstruction of the lowermost layer is wrong due to discretization errors.

To investigate the numeric behavior of XTT on more complex objects, experiments on the rope phantom for two different sets of scatter directions (N=13 and N=20) were performed. Generally, the reconstructions are in good accordance with the ground-truth data. At the object boundaries and at specific regions with high curvature and a rapidly changing scatter distribution, deviations from the ground-truth are observed for both N=13 and N=20. Hereby, N=13 seems to provide a slightly better reconstruction compared to N=20, which is probably due to a better step length

choice in the gradient descent. During our experiments we found that the optimal step lengths depends crucially on the particular set of scatter directions.

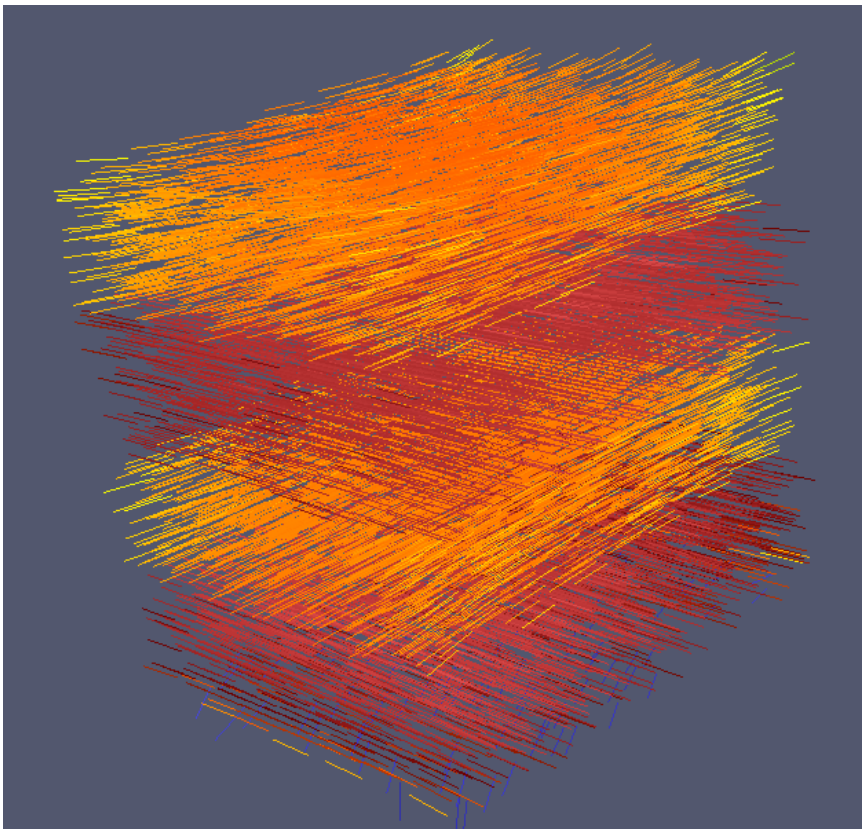

Figure 5.1: Reconstruction of the wooden-block phantom.

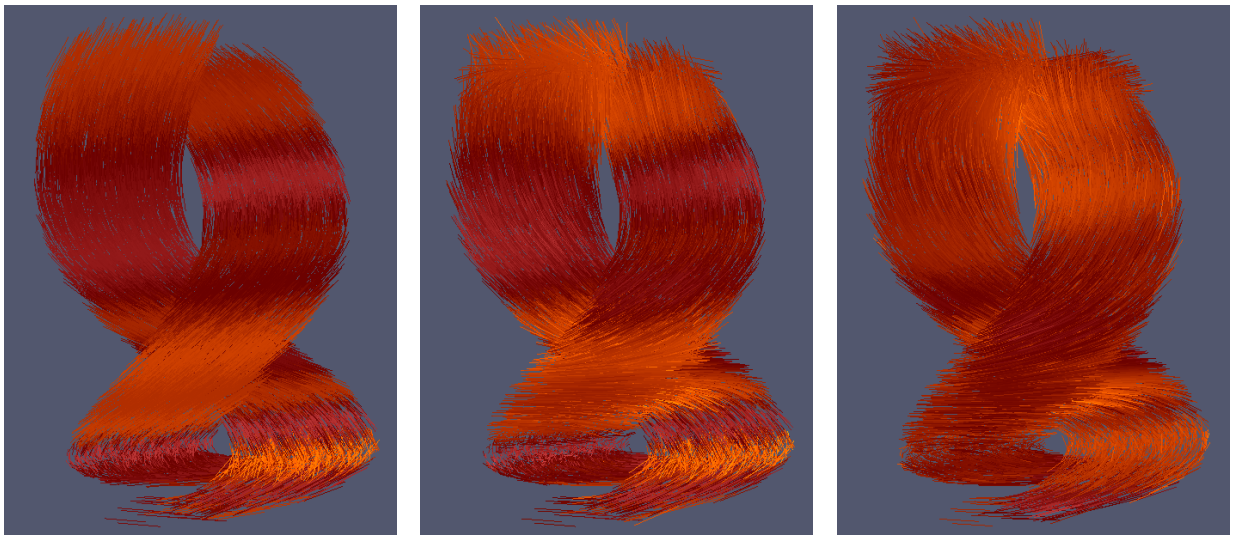

(a) Ground truth (b) Reconstruction N = 13 (c) Reconstruction N = 20

Figure 5.2: Visualization of the rope phantom. (a) ground-truth, (b) and (c) reconstruction with $N = 13$ and $N = 20$ scatter directions

5.2 Gradient Descent Analysis

In this work XTT was performed with the zero-constrained gradient descent method. Since reconstruction of both phantoms with only two trajectories has not been proper for all regions, we have analyzed the convergence of the gradient descent for the wooden-block phantom. In figure 5.3 we plotted the residual error of the gradient descent, thus the difference between the dark-field images and the forward-projected reconstruction result. The gradient descent convergences quickly in the first couple of iterations but does not improve significantly for iteration numbers larger then 25.

Probable reasons for the improper reconstruction are: First, the zero-constrain comes together with a non-steady transition at the object's boundaries, which is unnatural and hinders the gradient descent to converge to valid values at the boundary. Second, the optimal step length of the gradient descent is unknown and cannot be estimated easily. Better results are expected if more sophisticated reconstruction algorithms are used.

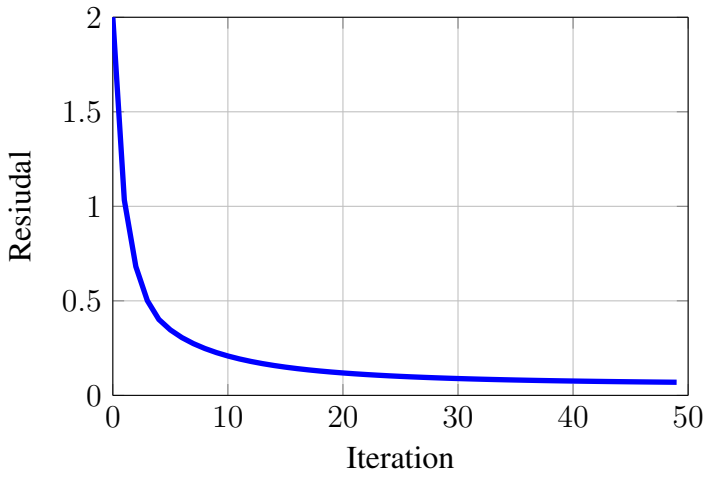

Figure 5.3: Residual error of the gradient descent XTT.

5.3 Influence of Scatter Directions

Since we are working on phantom data, the measures of the normalized residual norms and normalized mean updates, as introduced in Vogel [4], are not the best suited. Instead, we propose the mean angular deviation of the reconstructed tensor's smallest eigenvector $\boldsymbol{\alpha}_r^i$ to its respective one in the well-defined phantom $\boldsymbol{\alpha}_p^i$ over all voxel elements N:

$$\bar{\alpha} = \frac{1}{N} \sum_{i}^{N} \left|\left| \boldsymbol{\alpha}_p^i - \boldsymbol{\alpha}_r^i \right|\right|, \tag{5.1}$$

In the following, we will interpret the smallest half-axes of the reconstructed scattering ellipsoids as fiber directions. We want to stress that this assumption is still a matter of research and should be handled with care if applied on real data.

We evaluated the reconstruction result with the mean angle deviation for different sets of scatter directions. The reconstruction result of the wooden-block sample is shown in figure 5.4.

The error is significant larger for numbers below 4, which is understandable because no meaningful tensorial data can be fitted. For numbers between 4 and 8 the error is reduced but takes more or less the same value. Beginning with 9 directions the error drops again significantly and provides reasonable results. Generally the error decreases with a growing number of scatter directions, but the improvement is comparably low.

We conducted the same experiment with the rope-phantom, see figure 5.5, and experienced similar behavior. The error is high for low numbers of scatter vectors and drops off quickly to a first plateau at 8 scatter vectors. A second significant drop off is observed at 15 scatter vectors,

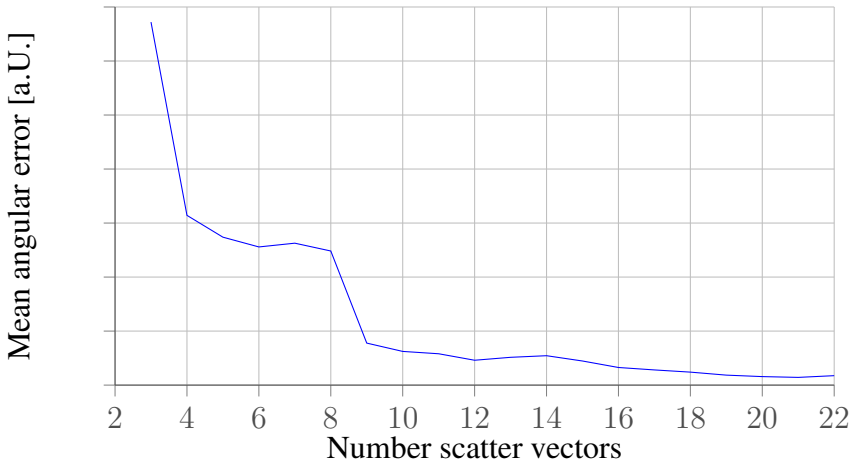

Figure 5.4: Reconstruction error for the wooden-block phantom.

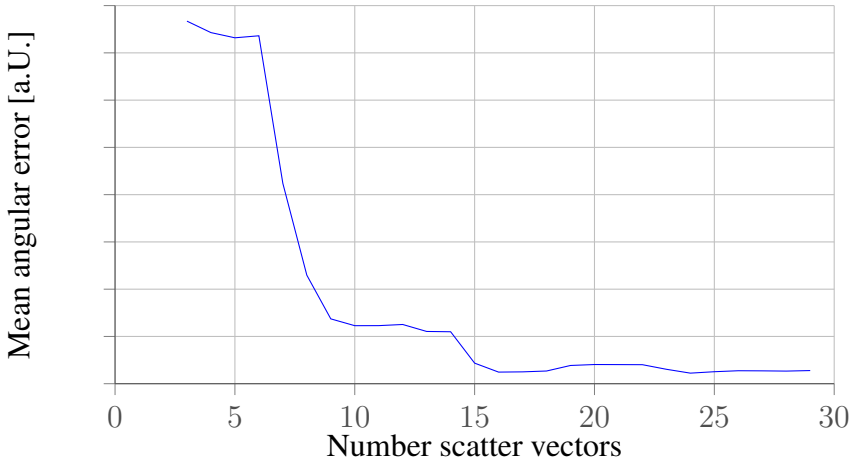

Figure 5.5: Reconstruction error for the rope phantom.

while no further improvement is visible for higher numbers.

Chapter 6

Discussion and Outlook

6.1 Discussion

In this paper we analyzed XTT by using well-defined phantom data [3, 4]. We have shown that reconstruction is generally possible with just two tomographic scans available, which enables recovering of tensorial data with a simpler laboratorial setup than proposed in Malecki. The algorithm has been adapted using a gradient descent method with a zero constraint.

Using the work of Saff [24] to sample an arbitrary number of scatter directions on a hemisphere, we have been able to analyze the influence of the number of scatter directions on the reconstruction results. For the used phantoms the accuracy between 7 scatter directions and 13 was evident. For higher number of scatter directions the results have shown to still improve slightly, but the cost of higher processing time does not justify usage of significantly higher numbers of scatter directions.

While the general results are in good accordance with ground-truth data we observed particular regions in the phantom, where no proper reconstruction of the fiber direction was possible. Up to this point, we have not been able to deduce the cause. We have two assumptions: First, the implemented adaption of the gradient descent could behave disadvantageous due to a bad step length choice or unsteadiness in the zero-constrains. Or secondly, and this would have more severe consequences for future clinical applicability, that two tomographic trajectories do not suffice for reconstructions.

6.2 Outlook

For future work, we are aiming to adapt the algorithm on real data. With an improved algorithm, a further going comparison between XTT and the method proposed by Hu et al. [1] can be

performed. Real data analysis with the laboratory setup proposed by Bayer [2] is not yet possible due to missing calibration of the geometrical setup.

For this reason it was not possible to register real data datasets successfully. Also, since the noise level is predominant in the real data dark-field projections, a further objective is to evaluate the phantom results under presence of noise.

Another aim is to adapt the geometry to a helical one, in the same manner as already known due to by absorption CT, see [29] or recently published by Marschner et al. [30] for phase contrast CT. This may provide a faster acquisition time and would be a subsequent step to clinical application.

List of Figures

1.1 Example for x-ray grating interferometric imaging 4

3.1 Absorption CT of the wooden-block sample 10

4.1 Random hemisphere sampling 12
4.2 Wooden block phantom 14
4.3 Sinogram of wooden-block phantom 16
4.4 dark-field images of the rope phantom for trajectory 1. 16
4.5 dark-field images of the rope phantom for trajectory 2. 17

5.1 Reconstruction of wooden-block phantom 20
5.2 Reconstruction of rope phantom 21
5.3 Residual error of the gradient descent XTT. 22
5.4 Reconstruction error for the wooden-block phantom. 23
5.5 Reconstruction error for the rope phantom. 23

Bibliography

[1] S. Hu, C. Riess, J. Hornegger, P. Fischer, F. Bayer, T. Weber, G. Anton, and A. Maier, "3-d tensor reconstruction in x-ray dark-field tomography - the first phantom result," in *Bildverarbeitung für die Medizin 2015* (H. Handels, T. Deserno, H.-P. Meinzer, and T. Tolxdorff, eds.), Informatik aktuell, (Berlin Heidelberg), 2015.

[2] F. L. Bayer, S. Hu, A. Maier, T. Weber, G. Anton, T. Michel, and C. P. Riess, "Reconstruction of scalar and vectorial components in x-ray dark-field tomography," *Proceedings of the National Academy of Sciences of the United States of America*, vol. 111, no. 35, pp. 12699–12704, 2014.

[3] A. Malecki, G. Potdevin, T. Biernath, E. Eggl, K. Willer, T. Lasser, J. Maisenbacher, J. Gibmeier, A. Wanner, and F. Pfeiffer, "X-ray tensor tomography," *EPL (Europhysics Letters)*, vol. 105, no. 3, p. 38002, 2014.

[4] J. Vogel, F. Schaff, A. Fehringer, C. Jud, M. Wieczorek, F. Pfeiffer, and T. Lasser, "Constrained x-ray tensor tomography reconstruction," *Optics Express*, vol. 23, no. 12, p. 15134, 2015.

[5] J. W. Goodman, *Introduction to Fourier optics*. Englewood, Colo.: Roberts & Co, 3rd ed. ed., 2005.

[6] U. Bonse and M. Hart, "An x-ray interferometer with long separated interfering beam paths," *Applied Physics Letters*, vol. 7, no. 4, p. 99, 1965.

[7] V. N. Ingal and E. A. Beliaevskaya, "X-ray plane-wave topography observation of the phase contrast from a non-crystalline object," *Journal of Physics D: Applied Physics*, vol. 28, no. 11, pp. 2314–2317, 1995.

[8] T. J. Davis, D. Gao, T. E. Gureyev, A. W. Stevenson, and S. W. Wilkins, "Phase-contrast imaging of weakly absorbing materials using hard x-rays," *Nature*, vol. 373, no. 6515, pp. 595–598, 1995.

[9] D. Chapman, W. Thomlinson, R. E. Johnston, D. Washburn, E. Pisano, N. Gmür, Z. Zhong, R. Menk, F. Arfelli, and D. Sayers, "Diffraction enhanced x-ray imaging," *Physics in Medicine and Biology*, vol. 42, no. 11, pp. 2015–2025, 1997.

[10] S. C. Mayo, T. J. Davis, T. E. Gureyev, P. R. Miller, D. Paganin, A. Pogany, A. W. Stevenson, and S. W. Wilkins, "X-ray phase-contrast microscopy and microtomography," *Optics Express*, vol. 11, no. 19, p. 2289, 2003.

[11] F. Pfeiffer, T. Weitkamp, O. Bunk, and C. David, "Phase retrieval and differential phase-contrast imaging with low-brilliance x-ray sources," *Nature Physics*, vol. 2, no. 4, pp. 258–261, 2006.

[12] C. David, B. Nöhammer, H. H. Solak, and E. Ziegler, "Differential x-ray phase contrast imaging using a shearing interferometer," *Applied Physics Letters*, vol. 81, no. 17, p. 3287, 2002.

[13] A. Momose, W. Yashiro, Y. Takeda, Y. Suzuki, and T. Hattori, "Phase tomography by x-ray talbot interferometry for biological imaging," *Japanese Journal of Applied Physics*, vol. 45, no. 6A, pp. 5254–5262, 2006.

[14] G. L. Zeng, *Medical image reconstruction: A conceptual tutorial / Gengsheng Lawrence Zeng*. Berlin and London: Springer, 2010.

[15] M. Bech, O. Bunk, T. Donath, R. Feidenhans'l, C. David, and F. Pfeiffer, "Quantitative x-ray dark-field computed tomography," *Physics in medicine and biology*, vol. 55, no. 18, pp. 5529–5539, 2010.

[16] T. H. Jensen, M. Bech, I. Zanette, T. Weitkamp, C. David, H. Deyhle, S. Rutishauser, E. Reznikova, J. Mohr, R. Feidenhans'l, and F. Pfeiffer, "Directional x-ray dark-field imaging of strongly ordered systems," *Physical Review B*, vol. 82, no. 21, 2010.

[17] F. Pfeiffer, C. Kottler, O. Bunk, and C. David, "Hard x-ray phase tomography with low-brilliance sources," *Physical review letters*, vol. 98, no. 10, p. 108105, 2007.

[18] A. Momose, W. Yashiro, S. Harasse, and H. Kuwabara, "Four-dimensional x-ray phase tomography with talbot interferometry and white synchrotron radiation: dynamic observation of a living worm," *Optics express*, vol. 19, no. 9, pp. 8423–8432, 2011.

[19] D. F. Swinehart, "The beer-lambert law," *Journal of Chemical Education*, vol. 39, no. 7, p. 333, 1962.

[20] V. Revol, C. Kottler, R. Kaufmann, A. Neels, and A. Dommann, "Orientation-selective x-ray dark field imaging of ordered systems," *Journal of Applied Physics*, vol. 112, no. 11, p. 114903, 2012.

[21] A. Malecki, G. Potdevin, T. Biernath, E. Eggl, E. Grande Garcia, T. Baum, P. B. Noël, J. S. Bauer, F. Pfeiffer, and R. L. Patterson, "Coherent superposition in grating-based directional dark-field imaging," *PLoS ONE*, vol. 8, no. 4, p. e61268, 2013.

[22] V. Revol, B. Plank, R. Kaufmann, J. Kastner, C. Kottler, and A. Neels, "Laminate fibre structure characterisation of carbon fibre-reinforced polymers by x-ray scatter dark field imaging with a grating interferometer," *NDT & E International*, vol. 58, pp. 64–71, 2013.

[23] I. T. Jolliffe, *Principal component analysis*. Springer series in statistics, Berlin and London: Springer, 2nd ed. ed., 2002.

[24] E. B. Saff and A. B. J. Kuijlaars, "Distributing many points on a sphere," *The Mathematical Intelligencer*, vol. 19, no. 1, pp. 5–11, 1997.

[25] L. A. Feldkamp, G. Jesion, and D. J. Kubinski, "Fundamental aspects of micro-ct in cone-beam geometry," in *Review of Progress in Quantitative Nondestructive Evaluation* (D. O. Thompson and D. E. Chimenti, eds.), pp. 381–388, Boston, MA: Springer US, 1989.

[26] J. Nuyts, B. de Man, J. A. Fessler, W. Zbijewski, and F. J. Beekman, "Modelling the physics in the iterative reconstruction for transmission computed tomography," *Physics in Medicine and Biology*, vol. 58, no. 12, pp. R63–R96, 2013.

[27] A. Malecki, G. Potdevin, and F. Pfeiffer, "Quantitative wave-optical numerical analysis of the dark-field signal in grating-based x-ray interferometry," *EPL (Europhysics Letters)*, vol. 99, no. 4, p. 48001, 2012.

[28] A. Ritter, P. Bartl, F. Bayer, K. C. Gödel, W. Haas, T. Michel, G. Pelzer, J. Rieger, T. Weber, A. Zang, and G. Anton, "Simulation framework for coherent and incoherent x-ray imaging

and its application in talbot-lau dark-field imaging," *Optics Express*, vol. 22, no. 19, p. 23276, 2014.

[29] W. A. Kalender, W. Seissler, E. Klotz, and P. Vock, "Spiral volumetric ct with single-breath-hold technique, continuous transport, and continuous scanner rotation," *Radiology*, vol. 176, no. 1, pp. 181–183, 1990.

[30] M. Marschner, M. Willner, G. Potdevin, A. Fehringer, P. B. Noël, F. Pfeiffer, and J. Herzen, "Helical x-ray phase-contrast computed tomography without phase stepping," *Scientific Reports*, vol. 6, p. 23953, 2016.